ADVANCED FUNCTIONAL MATERIALS
www.afm-journal.de

Laser Thermal Shock Enabling Ultrafast Spin Regulation of MnO_2 for Robust Pseudocapacitive Energy Storage

Yi Wan, Tong Cao, Yanan Li, Bin Wang, Wanli Wang, Yujie Xu, Hao Yang, Dongqing Zhang, Daliang Zhang, Qiang Li, Chang Yu, Han Hu,* and Mingbo Wu**

The pseudocapacitive performance of MnO_2 is intrinsically determined by its electronic structure, especially the spin state. However, the correlation between the electrochemical behavior and the spin state of electrode materials remains ill-defined, and efficient spin regulation strategies for MnO_2 are thus lacking. Herein, the study reports laser thermal shock of electrochemically deposited MnO_2 for efficient spin regulation. The combined use of theoretical calculation and experimental investigation indicates that the thermal shock induces oxygen vacancy in MnO_2 to reduce spin polarization and delocalize electron distribution. As a result, the electrical conductivity largely increases and the Na^+ adsorption is reasonably optimized. By lasering an integrated electrode for only 83 s, a 54% increase of the specific capacitance is observed. For the first time, the pseudocapacitive capability of MnO_2 is revealed by in situ electron paramagnetic resonance where the enhanced redox pair is correlated with evolution of Mn^{2+} during charge/discharge. Moreover, the commercial-level mass-loaded electrode also offers a decent performance enhancement after laser treatment, indicating the great prospect of this technology for real applications. This work innovatively correlates the pseudocapacitive performance of MnO_2 with its spin state and offers a new avenue to optimize the electrochemical capability through spin regulation.

1. Introduction

Electrochemical energy storage devices have aroused increasing attention because of their critical role in the upcoming electrified society.[1] Apart from the predominant lithium-ion batteries, supercapacitors (SCs) featuring rapid charge/discharge rates also demonstrate indispensable status due to their capability for high-power applications.[2] However, the commercially available SCs, using porous carbon electrode materials based on the electric double-layer mechanism, offer an extremely low energy density. As a result, tremendous efforts have been devoted to searching for alternative electrode materials for SCs. Among them, transitional metal oxides (TMOs) with surface redox reactions, for example, MnO_2, have been actively pursued.[3] In a typical pseudocapacitive process of MnO_2, the cations, such as Na^+, in the electrolyte could intercalate into the lattice of MnO_2 at the near-surface region, accompanying electron transfer for energy storage.[4] In this regard, the electron/Na^+ diffusion behavior within MnO_2 plays an essential role in determining its electrochemical performance, which is intrinsically related to its electronic configuration, especially the spin state.[5] Nevertheless, the correlation between the pseudocapacitive performance and the spin state of MnO_2 is insufficiently revealed. In consequence, the rules and regularities capable of fundamentally boosting the electrochemical property of MnO_2 remain to be systematically investigated.

Y. Wan, Y. Li, B. Wang, W. Wang, Y. Xu, H. Yang, D. Zhang, H. Hu, M. Wu
State Key Laboratory of Heavy Oil Processing
Institute of New Energy
College of Chemistry and Chemical Engineering
China University of Petroleum (East China)
Qingdao 266580, China
E-mail: hhu@upc.edu.cn; wumb@upc.edu.cn

T. Cao, D. Zhang
Multi-scale Porous Materials Center
Institute of Advanced Interdisciplinary Studies
School of Chemistry and Chemical Engineering
Chongqing University
Chongqing 400044, China
E-mail: daliang.zhang@cqu.edu.cn

Q. Li
College of Physics
Center for Marine Observation and Communications
Qingdao University
Qingdao 266071, China

C. Yu
State Key Lab of Fine Chemicals
School of Chemical Engineering
Liaoning Key Lab for Energy Materials and Chemical Engineering
Dalian University of Technology
Dalian 116024, China

The ORCID identification number(s) for the author(s) of this article can be found under https://doi.org/10.1002/adfm.202311157

DOI: 10.1002/adfm.202311157

Since the pioneering work of Shao-Horn et al., the relationship between the spin state and electrocatalytic capability of TMOs has been intensively investigated.[6] As revealed by the current progress, the spin state transition of TMOs can directly regulate the strength of metal-ligand bonds and optimize adsorption toward reactive species for improved catalytic performance.[7] Up to now, tremendous strategies including defects introduction,[8] size regulation,[9] lattice doping,[10] and metal-support interaction,[11] etc., have been proposed to regulate the spin state. These technologies share the common point that the local symmetry of TMOs is destroyed to induce spin state transition. Because of the similarity between electrochemical energy storage and electrocatalysis, the identical regulation rules may also be effective in pseudocapacitive materials. As for MnO_2, one of the most straightforward and potential processes for spin regulation will be to introduce oxygen vacancies (OVs) in the electrode material. Thus, a clear understanding of the influence of OVs on the spin state of MnO_2 will be of paramount importance in establishing effective methods to improve the electrochemical performance of MnO_2. Moreover, it will be more meaningful if the related means could be directly applied to electrodes with commercial-level mass-loading.

Herein, laser irradiation is applied to the electrochemically deposited MnO_2 to produce a material platform, of which the spin state on the pseudocapacitive performance is theoretically and experimentally investigated. The irradiation could induce thermal shock to create OVs within MnO_2. Theoretical investigation reveals that OVs delocalize the electron distribution and reduce the spin polarization, via which the bandgap and adsorption behavior toward Na^+ are rationally regulated. After treating the MnO_2-based electrode for several tens of seconds at an optimal condition, a 54% increase of the specific capacitance is afforded, demonstrating extremely high efficiency of the laser thermal shock means. Then, the correlation between the intrinsically enhanced electrochemical performance and the spin state of MnO_2 has been revealed by in situ electron paramagnetic resonance (EPR) where the enhanced redox capability could be directly correlated with variation of spin-polarized Mn^{2+}. Moreover, the laser thermal shock could be directly applied to the commercial-level mass-loaded electrodes, and 20% increase of the specific capacitance is achieved by lasering the high-mass loaded electrodes. The thick MnO_2-based electrode is used to construct a hybrid supercapacitor (HSC), delivering an energy density of 2.54 mW h cm^{-3} at a power capability of 19.36 mW cm^{-3}. The findings discovered in this work may shed new light on the correlation between electrochemical performance and spin state of MnO_2 as well as contribute to a totally new strategy for regulating the performance of pseudocapacitive materials.

2. Results and Discussion

To reveal the influence of OVs on the spin state and pseudocapacitive performance of MnO_2, density functional theory (DFT) calculation has been carried out. The typical modes of MnO_2 and MnO_2 with OV (MnO_{2-x}) were built and shown in Figure S1 (Supporting Information). **Figure 1**a,b compare the total densities of states (DOS) and the projected DOS (PDOS) of MnO_2 (Figure 1a) and MnO_{2-x} (Figure 1b). Both structures consist of high spin-up polarized electrons near the Fermi level, but the spin-down ones that originate from the d_{xy} electrons (Figure S2, Supporting Information) are only observed in MnO_{2-x} in the corresponding region. Because of regulated electron distribution, the spin polarization of MnO_{2-x} could be reduced (Table S1, Supporting Information), which could facilitate the adsorption/desorption and transfer process of electrolyte ions.[12] The calculated bandgap for the MnO_2 is 0.53 eV. As for the MnO_{2-x}, a new state is generated at ca. −0.25 eV above the valence band maximum (VBM) within the bandgap, leading to an essentially reduced bandgap of 0.36 eV, which enhances intrinsic electrical conductivity and charge transfer.[13] Since the new state is derived from Mn 3d spin-up and O 2p spin-up states, the OV could delocalize the neighboring electrons around the adjacent Mn atoms.[14] To reveal the effect of electron delocalization, the electron localization function (ELF) has been performed. As shown in Figure 1c,d, electron delocalization occurs around the OV site, which can promote electron transfer in the electrode materials.[15] As expected by PDOS in Figure S3 (Supporting Information), the 3d orbital of Mn and the 2p orbital of O overlap with the 3s orbital of Na, thus the transfer of itinerant e_g electrons is facilitated, providing the pseudocapacitive storage sites.[16] Moreover, the spin density distribution (Figure 1e,f) displays that the spin density weakens near the OV site, which is consistent with the DOS result. The adsorption energy (ΔE_{ads}) of Na^+ was further calculated to study the adsorption behavior at different slabs. Compared with that of the MnO_2 (−3.39 eV), the ΔE_{ads} of MnO_{2-x} has a thermoneutral value (−1.79 eV). The high ΔE_{ads} of MnO_2 results from the high spin-up polarized electrons at the VBM and these unpaired electrons at the 3d orbit of Mn offer strong adsorption of Na^+.[7b,17] The charge density difference of the two structures is compared in Figure 1g,h. As shown, Na^+ offers a stronger interaction with MnO_2, requiring more energy for the adsorbed ions to be desorbed.[18] On the other hand, the MnO_{2-x} has facilitated Na^+ adsorption/desorption, contributing to better pseudocapacitive performance. Based on these calculation results, the OV in MnO_2 results in a reduced spin polarization to decrease the bandgap and delocalize the electrons, which contributes to boosted electron transfer and improved electron cloud interaction. In this regard, the essentially improved electrochemical performance of MnO_2 with OVs is theoretically expected.

Inspired by the aforementioned theoretical observation, OVs were controllably introduced into the framework of MnO_2 through a computer-aided laser process. As an intensified light illumination, laser induces extremely strong electron and molecule motions of the irradiated materials. In this regard, the localized lattice vibration is realized to achieve a rapid temperature rise for structure regulation.[19] Specifically, MnO_2 nanosheets were electrochemically deposited on the carbon cloth (CC) irradiated by laser in advance at ambient atmosphere (Figure S4, Supporting Information), which were then scanned with laser beam (**Figure 2**a) for seconds (Video S1, Supporting Information) to regulate local structure in an inert atmosphere (Figure S5, Supporting Information). The laser irradiation induces a transient thermal shock (Figure S6, Supporting Information) rendering the CC a super-hydrophilic surface (Figures S7–S10 and Table S2, Supporting Information), benefiting a uniform MnO_2 loading.[20] As shown in Figure S11 (Supporting Information), the optimized laser-irradiated CC permits a commercial-level mass loading of ≈10 mg cm^{-2}. An interesting finding is

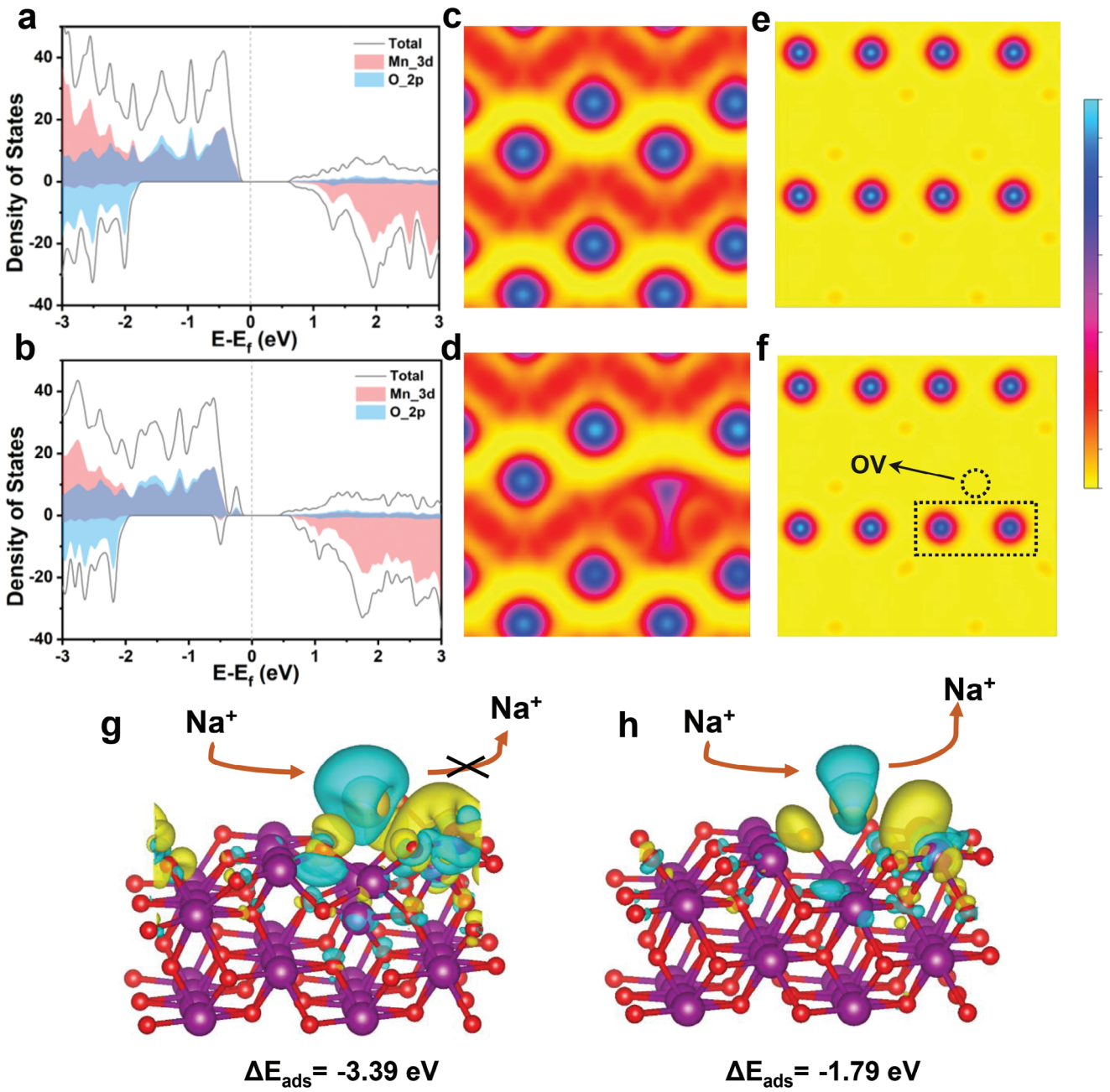

Figure 1. DOS of a) MnO_2 and b) MnO_{2-x}. ELF and spin density distribution of c,e) MnO_2 and d,f) MnO_{2-x}, respectively. Charge density difference of g) MnO_2 and h) MnO_{2-x}, in which yellow and cyan areas represent charge accumulation and depletion, respectively. The isosurface is set to 0.0015 e Bohr^{-3}.

that the overpotential for electrochemical deposition of MnO_2 is largely reduced (Figure S11a, Supporting Information) on the laser-irradiated CC.[21] As for the structure evolution of MnO_2 under laser irradiation, the numerical simulation (Figure 2b) demonstrates that the irradiated surface can be heated to an extremely high temperature in a very short duration. In this regard, the strong lattice vibration is realized. A reconstruction of the local structure is thus achieved, mainly in the form of releasing some oxygen to produce vacancies, after the subsequent quenching during the laser scanning process.[22] The laser-irradiated MnO_2 (L-MnO_2) shows decreased intensity in its X-ray diffraction (XRD) pattern (Figure 2c; Figure S12, Supporting Information), but its microstructure is well-maintained (Figure 2d; Figure S13a–c, Supporting Information) except for the introduction of defects within the framework of nanosheets (Figure 2e,f; Figure S13d–f, Supporting Information). Energy-dispersive spectroscopy (EDS) mapping (Figures S14 and S15, and Table S3, Supporting Information) reveals that the signal intensity of oxygen in L-MnO_2 is slightly reduced, indicative of incorporating OVs within the frameworks of L-MnO_2. To further confirm

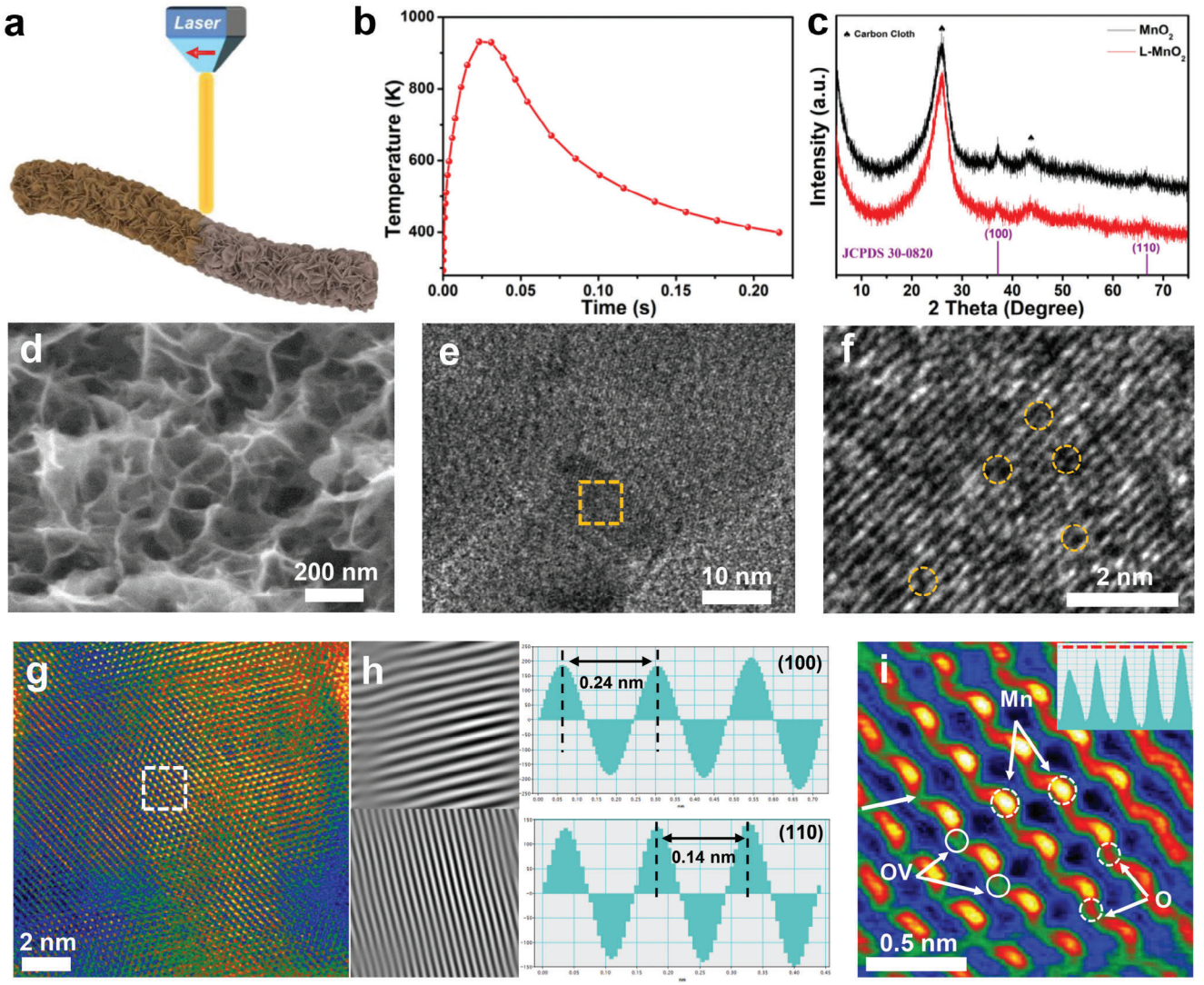

Figure 2. a) Schematic diagram of producing L-MnO_2. b) Simulated thermal evolution as a function of time on the surface of MnO_2. c) XRD patterns of MnO_2 and L-MnO_2, d) Scanning electron microscopy (SEM), e) Transmission electron microscopy (TEM), f) High-resolution TEM of L-MnO_2 g) HAADF-STEM image of L-MnO_2 and h) FFT patterns of the area marked by a white rectangular in (g). i) The corresponding filtered image of the white square in (g) and the insert showing the normalized intensity variation of columns of O atoms along the arrow.

this structural evolution, high-angle annular dark field scanning transmission electron microscopy (HAADF-STEM) of L-MnO_2 is conducted, as shown in Figure 2g. The bright dots reveal the arrangement of Mn atoms and the fast Fourier transform (FFT) patterns (Figure 2h) clearly indicate the (100) and (110) planes of MnO_2. Figure 2i magnifies the marked region (Figure 2g) suggesting the missed connection between Mn atoms, which could be identified as OVs.

To have a clear understanding of OVs via laser scanning, explicit spectral characterizations have been conducted. The X-ray photoelectron spectroscopy (XPS) spectra of MnO_2 and L-MnO_2 in the region of Mn 2p, Mn 3s, and O 1s were deconvoluted and compared in **Figure 3**a–c and Figure S16 (Supporting Information). As shown in Figure 3a, L-MnO_2 contains more low-valence Mn and its content could be regulated through modulating laser power (Figure S16b, Supporting Information).[23] In this regard, the average oxidation state of L-MnO_2, obtained from Mn 3s spectra (Figure 3b; Figure S16c and Table S4, Supporting Information), is reduced by 8.3% compared to the original one. A decrease in Mn valence is capable of preserving the total charge conservation when OVs are incorporated in the MnO_2 lattice.[24] The O 1s spectra in Figure 3c and Figure S16d (Supporting Information) show three peaks at 529.7, 531.2, and 532.6 eV, corresponding to the lattice oxygen ($O_{lattice}$), OVs, and adsorbed water (O_{water}), respectively.[25] Reduced content of $O_{lattice}$ but increased OVs is observed after laser scanning, consistent with the variation of Mn spectra. Furthermore, the UV-vis diffuse reflection spectroscopy verifies that the bandgap of L-MnO_2 decreases (Figure S17, Supporting Information), agreeing well with the DFT calculation result. Then, X-ray absorption spectroscopy (XAS) was employed to uncover the local structural evolution caused by OVs. The main peak of the Mn *K*-edge for MnO_2 is located

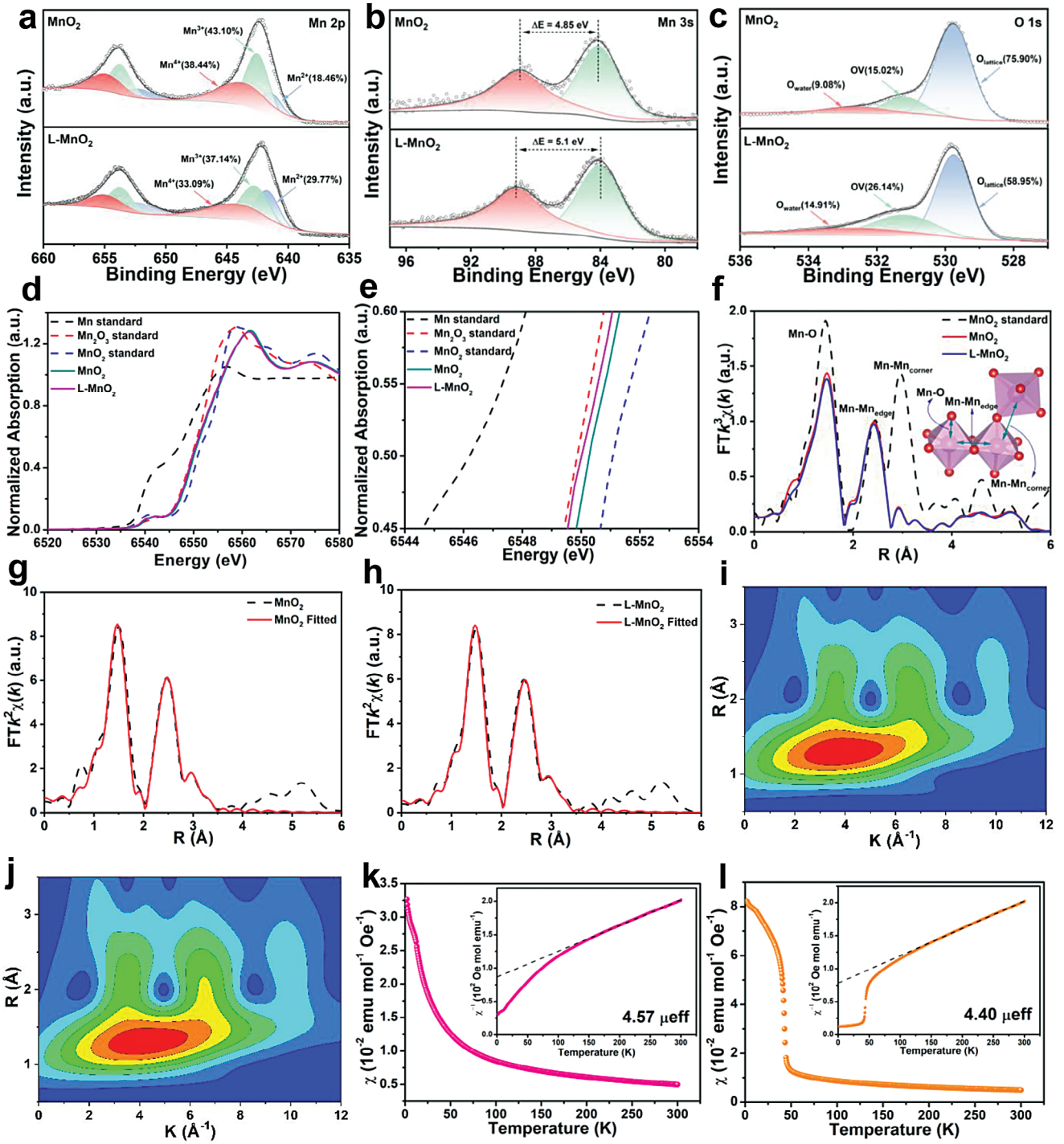

Figure 3. High-resolution XPS spectra of a) Mn 2p, b) Mn 3s, and c) O 1s of MnO_2 and L-MnO_2. d) Mn *K*-edge X-ray absorption near edge structure (XANES) spectra and e) the corresponding magnified region of MnO_2 standard, Mn_2O_3 standard, Mn standard, MnO_2, and L-MnO_2. f) Radial distribution functions of both MnO_2 standard, MnO_2, and L-MnO_2. EXAFS signal fitting curves in *k*-space between 1 to 3.2 Å for g) MnO_2 and h) L-MnO_2. WT contour plots of i) MnO_2 and j) L-MnO_2. Magnetic susceptibility of k) MnO_2 and l) L-MnO_2.

between that of Mn^{3+} (Mn_2O_3) and Mn^{4+} (MnO_2) (Figure 3d,e), suggesting that Mn is dominated in the form of Mn^{4+}. As for L-MnO_2, the main peak at the Mn *K*-edge shifts to lower energy, indicating the valence state reduction of Mn. Figure 3f displays the corresponding Fourier transform (FT) of the Mn *K*-edge $k^2\chi(k)$ spectra from the extended X-ray absorption fine structure (EXAFS). The peaks located at 1.5, 2.5, and 3.0 Å are indexed with Mn—O bond, Mn-Mn_{edge} bond (Mn—Mn in the edge-shared octahedra), and Mn—Mn_{corner} bond (Mn-Mn in the corner-shared octahedra) (Figure 3f insert), respectively.[26] The

reduction of the *K*-space oscillation around the 1–6 Å is observed for the L-MnO_2 (Figure S18, Supporting Information), suggesting the structure difference in the coordinative environment of Mn atom.[27] Figure 3g,h, and Table S5 (Supporting Information) illustrate the fitted k^3-weighted EXAFS date of MnO_2 FT at Mn *K*-edge. Obviously, the coordination number (CN) of Mn—O bond in L-MnO_2 (3.4) decreases compared to the MnO_2 (3.7), implying more OVs existing in L-MnO_2. The CN of Mn—Mn_{corner} bond in L-MnO_2 sample (2.2) increases compared to the MnO_2 (1.8). To verify this, the wavelet transform (WT) technology is performed in both *R* and *K* space to distinguish multiple-scattering. L-MnO_2 (Figure 3j) exhibits higher intensity at larger *K* spaces compared to MnO_2 standard (Figure S19, Supporting Information) and MnO_2 (Figure 3i), indicating fewer Mn—O bonds and more Mn—Mn_{corner} bonds. These binding conditions in the lattice contribute to different spin states. The Mn—Mn_{corner} favors the antiferromagnetic (AFM) configuration, while the Mn—Mn_{edge} benefits the ferromagnetic one. The AFM configuration features antiparallel spins, leading to a reduced spin polarization in L-MnO_2. To further unravel the change of electron spin configuration after laser treatment, the temperature-dependent magnetizations were measured. As confirmed in susceptibility measurement (Figure 3k,l), the calculated effective magnetic moment (μ_{eff}) of L-MnO_2 (4.40 μ_B) is smaller than that of MnO_2 (4.57 μ_B), indicating less unpaired *d* electron and low-spin state. A moderate spin polarization may harvest a mild adsorption process, facilitating reversible electrochemical reactions.[12]

To correlate the spin state and electrochemical performance of MnO_2, the pseudocapacitive performance of MnO_2 and L-MnO_2 (1.8 mg cm^{-2}) was evaluated in a three-electrode configuration. The MnO_2 electrodes offer a typical rectangular cyclic voltammogram (CV) curve (Figure S20, Supporting Information) with a pair of weak bumps due to the pseudocapacitive contribution.[28] As for L-MnO_2 electrode, a pair of obvious redox peaks could be observed, indicative of the essentially increased contribution from the surface redox reactions (**Figure 4**a).[29] The triangular galvanostatic charge/discharge (GCD) profiles are highly symmetrical while the curve of L-MnO_2 spans an almost 50% extended duration (Figure 4b). As revealed from Figure S13a (Supporting Information), the surface of the substrate is fully covered with the active species, and the capacitive contribution from the carbon-based current collectors, which is relatively small even without active species decoration (Figure S21, Supporting Information), could be excluded. This excellent regulation effect highlights the high efficiency of lasering process. The specific capacitance of the two electrodes at different current densities is compared in Figure 4c, where the L-MnO_2 offers a slower decrease rate of specific capacitance over the current density. Electrochemical impedance spectroscopy (EIS) was carried out to compare the kinetics behavior of the MnO_2 and L-MnO_2 electrodes. In the Nyquist plots (Figure 4d; Figure S22, Supporting Information), the L-MnO_2 exhibits a much smaller semicircle related to the charge-transfer resistance. In addition, the equivalent series resistance, associated with the electrical resistance of electrodes, is also much smaller for the L-MnO_2 electrode. The electrochemical kinetics was further analyzed to distinguish the ionic diffusion contribution and surface capacitive contribution.[30] Obviously, the contribution of the surface capacitance of MnO_2 (Figure 4e) and L-MnO_2 (Figure 4f) increases with the scan rate. Additionally, the diffusion control effect of L-MnO_2 is higher than that of MnO_2. These results suggest the positive effect of rationally regulated spin state on the Na^+ storage performance.[31]

To get an insight into the effect of spin state on the electrochemical performance, in situ and ex situ characterizations of the electrode at different states were evaluated. As shown in Figure 4g,h, the in situ Raman spectra feature three major regions for L-MnO_2 electrode during charge/discharge, at 642–662 (ν_1), 570–580 (ν_2), and 495–508 cm^{-1} (ν_3). The ν_1 (Mn—O) band can be attributed to the Mn—O symmetric stretching vibration along d_z^2 orbital of [MnO_6] octahedral, involving the Na^+ ions adsorption/desorption.[32] The ν_2 (Mn—O) band can be assigned to the stretching vibration along $d_{x^2-y^2}$ orbital in the basal plane of [MnO_6].[33] The ν_3 (Mn—O) band is a faint vibration of Mn—O bond, associated with the insertion/extraction of Na^+. During the charge process (Figure 4g), the intensities of ν_1 and ν_2 bands enhance slightly with the increase of the potential owing to the electrochemical oxidation from low-valanced $Mn^{2+/3+}$ to Mn^{4+}. A blue shift of the ν_3 band is observed, which is related to the Na^+ extraction from the amorphous region.[32] Inversely, the intensities of ν_1 and ν_2 bands decrease and the ν_3 band goes through a red shift as the decrease of potential during the discharge process (Figure 4h). However, all bands express significant red shift and blue shift at the potential of 0.5–0.6 V (charge) and 0.4–0.3 V (discharge), respectively. Typically, the presence of OVs leads to the red shift of the three bands, as shown in Figure S23 (Supporting Information).[18] In this regard, the intercalated Na^+ ions fill the OVs sites, which leads to the occupation of OVs and the blue shift of the three bands during the discharge. While the extraction of Na^+ ions regenerates OVs, leading to the red shift of these bands during the charge process. Then, the ex situ XRD (Figure S24, Supporting Information) was performed and negligible phase transition is observed, which is good agreement with the in situ Raman observation.[34] In addition, in situ EPR (Figure S25, Supporting Information) was also conducted during CV testing (Figure S26, Supporting Information). As shown in Figure 4i and Figure S27 (Supporting Information), six hyperfine lines centered at $g \approx 2.0$ were detected, which is the signature of isolated Mn^{2+} ions ($S = 5/2$, $I = 5/2$) belonging to $M_S = 1/2 \leftrightarrow M_S = -1/2$ transition.[35] The introduction of OVs within MnO_2 produces low-coordinated Mn, thus forming low-valanced Mn^{2+}. During the charge process, the peak intensity of EPR spectra decreases with the rise of the potential, attributing to the oxidation of Mn^{2+} to high-valanced Mn^{3+}/Mn^{4+}, and vice versa during the discharge process. An increased peak intensity is observed at the potential between 0.4 to 0.58 V (Figure 4j,k) during the charge process. The extraction of Na^+ from OVs sites produces the low-coordinated Mn, thus increasing Mn^{2+}. During the discharge, the insertion of Na^+ into OVs sites generates high-valance Mn and then causes the sharp decrease of Mn^{2+} concentration at the potential range of 0.45 to 0.3 V. These results also match well with the in situ Raman observation. Furthermore, the interactions between the framework and intercalated species in the absence/presence of OV within MnO_2 are investigated by the projected crystal orbital Hamilton population (COHP) (Figure S28a,b, Supporting Information). The negative and positive values of COHP suggest the bonding and anti-bonding interactions between Mn and Na. Figure S28c (Supporting Information) reveals that weak Mn-Na interaction in the MnO_2 below the Fermi

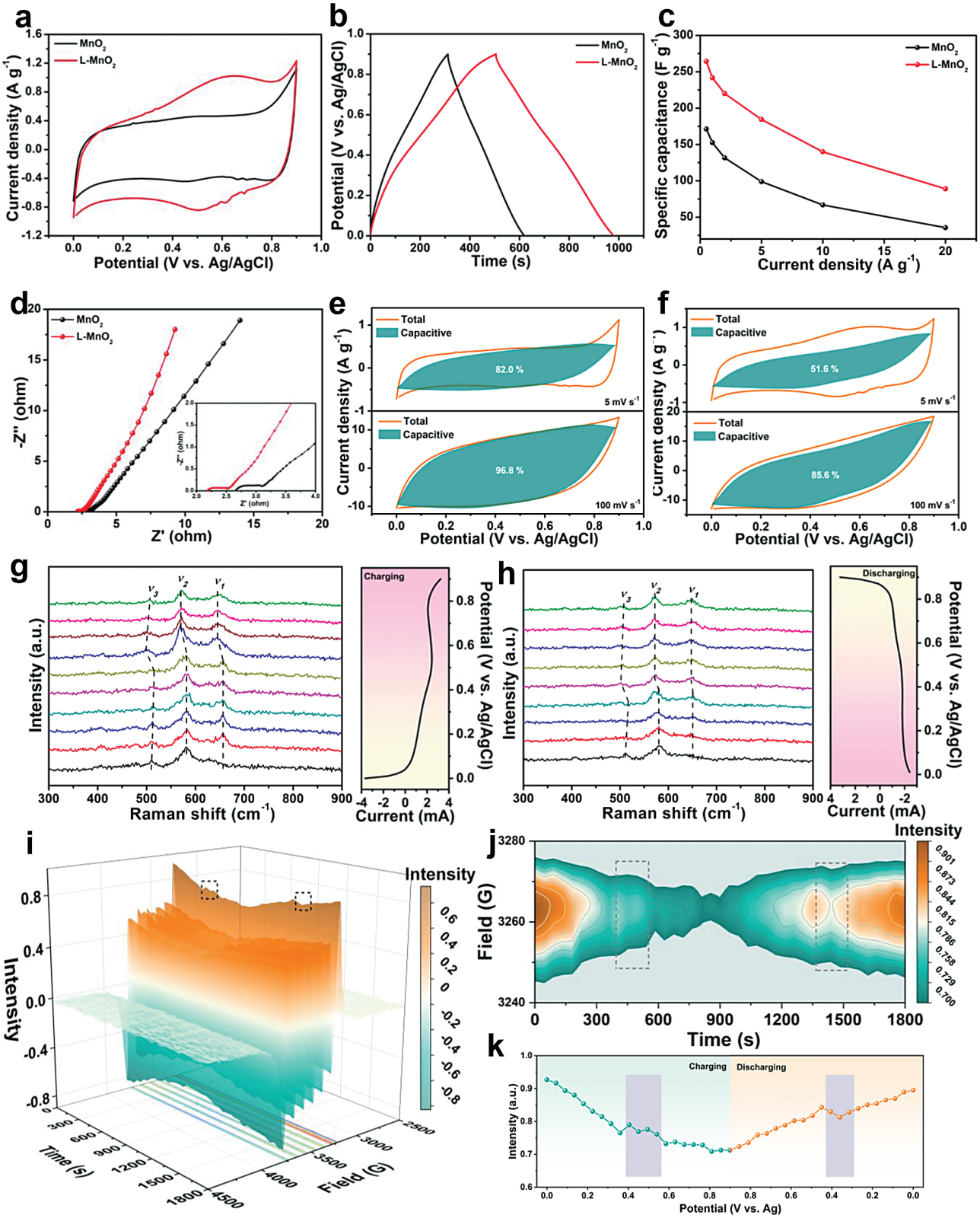

Figure 4. Electrochemical tests of MnO_2 and L-MnO_2: a) CV curves measured at a scan rate of 5 mV s^{-1}, b) GCD profiles recorded at a current density of 0.5 A g^{-1}, c) rate capability, d) Nyquist plots, e,f) the capacitance contribution at scan rates of 5 mV s^{-1} and 100 mV s^{-1}. In situ Raman spectra of the L-MnO_2 electrode during the g) charge and h) discharge. In situ EPR test of the L-MnO_2 electrode: i) the spectra between 2500 to 4500 G, j) magnified EPR spectra between 3240 to 3280 G, and k) evolution of the peak intensity.

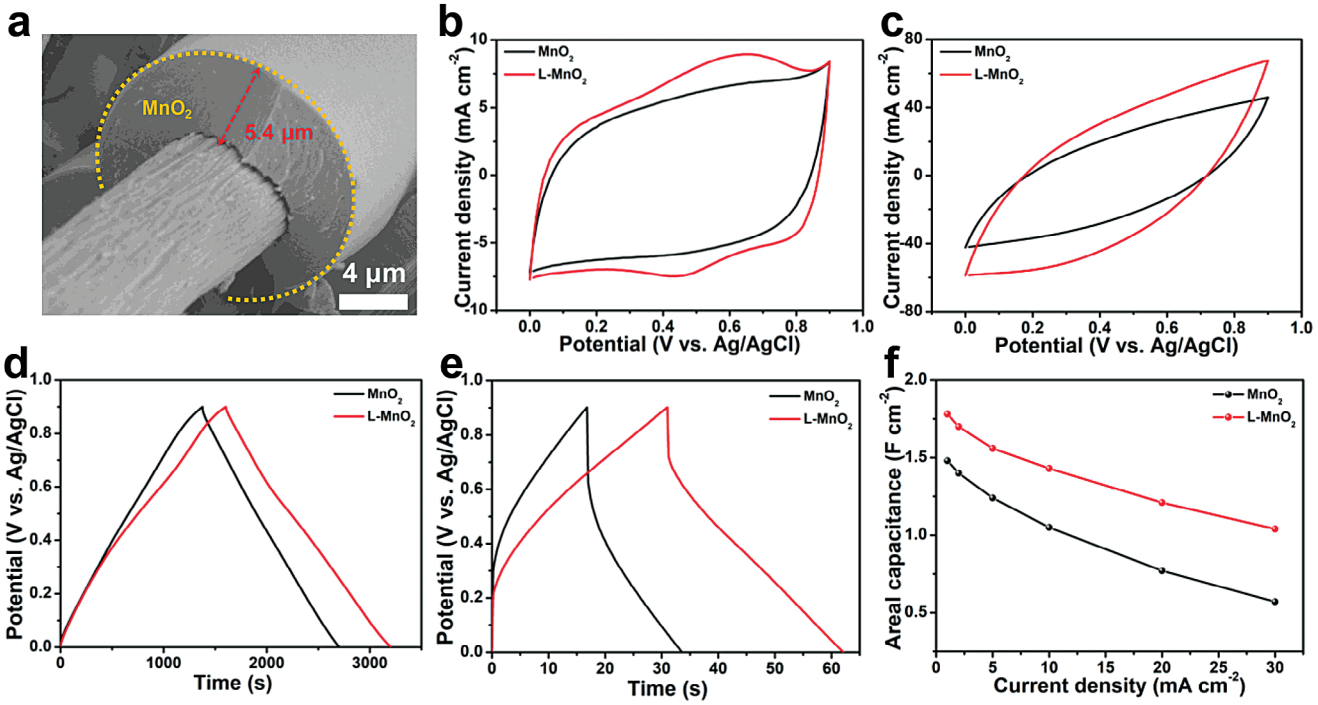

Figure 5. a) SEM image of a high-mass-loaded MnO_2 electrode after lasering. CV curves of MnO_2 and L-MnO_2 at scan rates of b) 5 mV s^{-1} and c) 50 mV s^{-1}. GCD profiles of MnO_2 and L-MnO_2 measured at the current densities of d) 1 mA cm^{-2} and e) 30 mA cm^{-2}. f) Rate capability of MnO_2 and L-MnO_2.

level, whereas the interaction is optimized in the MnO_{2-x} mainly due to the high spin electrons at ca. −0.4 to −3 eV (Figure S28d, Supporting Information). The integrated COHP (ICOHP) value between Mn and Na atom is −0.324 eV for the MnO_{2-x}, which is much more negative than that of MnO_2 (−0.081 eV) for facilitated charge transfer. In brief, the fast-redox action of Mn^{3+}/Mn^{4+}, collaborating with OVs facilitated insertion/extraction of Na^+, contributes to the preeminent capacitive capability.

The laser thermal shock was then further applied to commercial-level mass-loaded electrodes to demonstrate the feasibility of this technology in practical application. The MnO_2 electrode with a high mass loading could be achieved through extending the electrochemical deposition duration. After laser irradiation, the mass loading offers a minor variation but still could be high as ≈10 mg cm^{-2} (ca. 9.4 mg cm^{-2}), as shown in **Figure 5**a. Even for the thick electrode, L-MnO_2 still shows a 20% increase of the specific capacitance. Similar evolution in the CV curves is observed as compared to the low-mass loaded electrode in Figure 4a. At the high mass loading, the electrochemical performance of the electrode was compared in areal metrics. As shown in Figure 5b–f and Figure S29 (Supporting Information), very decent performance is achieved, compared favorably to most of the previously reported results (Table S6, Supporting Information). The detailed comparison of the high mass-loaded MnO_2 and L-MnO_2 suggests that the obviously larger areal capacitance of laser scanned electrode, demonstrating the effectiveness of the laser process. The SEM images of MnO_2 electrodes after the 3000th cycle display an apparent peeling off of the active species from the CC (Figure S30b,c, Supporting Information), while the active species of L-MnO_2 electrode are still firmly coated on the substrate (Figure S30d,e, Supporting Information). In a word, the laser scanning process could not only be applied to unravel the intrinsic behavior of the electrode materials, but also be directly extended to the commercial-level mass-loading electrodes for real application.

The laser-irradiated MnO_2 electrode was then used to construct HSCs by pairing with a VO_x anode, denoted as L-MnO_2//VO_x, as shown in **Figure 6**a. The detailed structural and electrochemical investigation of VO_x anode is shown in Figures S31 and S32 (Supporting Information). The working potential window of the two electrodes was determined through their CV curves and a suitable potential window of 0 to 0.9 V (versus Ag/AgCl) for the cathode and 0 to −1.1 V (versus Ag/AgCl) for the anode (Figure S33a, Supporting Information) was confirmed. In this regard, the HSCs could be operated in a voltage of 2 V as shown in Figure 6b. The GCD curves (Figure 6c) display a symmetrical feature and the volume capacitance reaches 4.58 F cm^{-3} at 2 mA cm^{-2}. The energy and power density of HSCs is shown in Figure 6d. Notably, the device achieves a high volume energy density of 2.54 mW h cm^{-3} at a power density of 19.36 mW cm^{-3} and 0.65 mW h cm^{-3} at 292.5 mW cm^{-3}, which is superior to many of the previously reported MnO_2-based supercapacitors.[36]

3. Conclusion

In summary, the spin state and pseudocapacitive performance of MnO_2 have been correlated by the theoretical and experimental investigation of OVs on the electrochemical evolution of MnO_2. The OVs could be efficiently introduced through a rapid laser thermal shocking process, which was confirmed by XAS, and HADDF-STEM measurement. A 54% increase of the

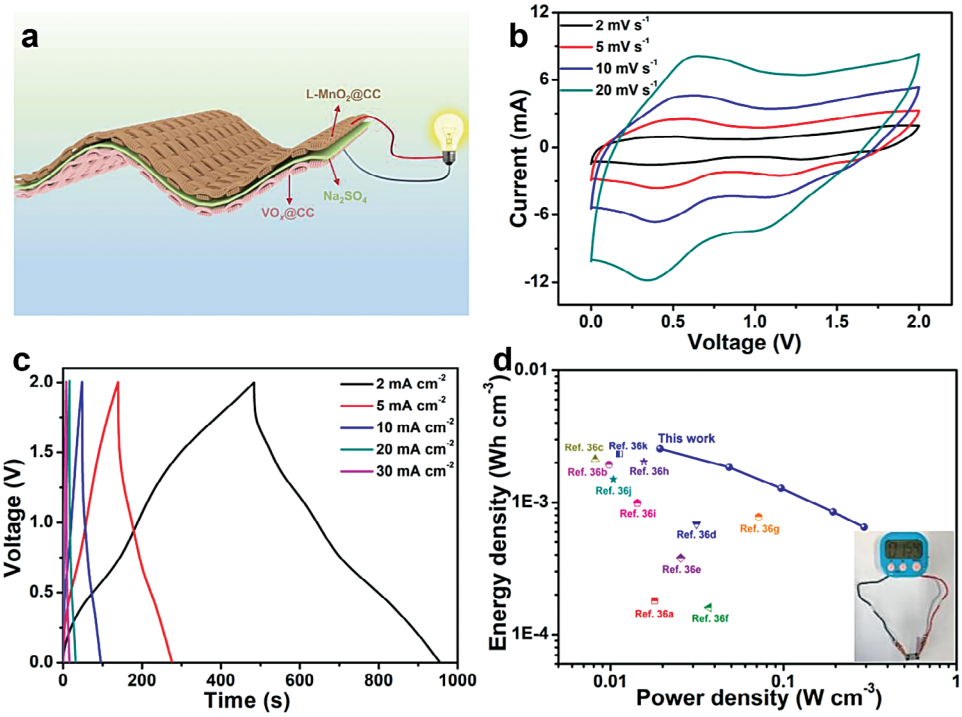

Figure 6. a) Schematic diagram of the HSC L-MnO_2//VO_x. b) CV curves of the L-MnO_2//VO_x at different scan rates. c) GCD curves of the L-MnO_2//VO_x at different current densities. d) Performance comparison of the L-MnO_2//VO_x with some recently reported HSCs (insert showing the electronic clock powered by L-MnO_2//VO_x).

specific capacitance was achieved by laser scribing the MnO_2 electrode for seconds. The effect of OVs on electrochemical performance has been revealed by in situ characterizations including EPR, demonstrating the high correlation with reduced spin polarization. Moreover, the laser treatment could also be applied to commercial-level mass-loaded electrodes, showing the potential for practical application. The HSCs assembled using the laser-irradiated MnO_2 offer an excellent capability, superior to most of the previous results. This work not only correlates the spin state and electrochemical performance of MnO_2 but also proposes a totally new spin regulation strategy to improve the performance of pseudocapacitive materials.

Supporting Information

Supporting Information is available from the Wiley Online Library or from the author.

Acknowledgements

The authors acknowledge the financial support from Shandong Provincial Natural Science Foundation (ZR2020ZD08) and China University of Petroleum (East China).

Conflict of Interest

The authors declare no conflict of interest.

Data Availability Statement

The data that support the findings of this study are available from the corresponding author upon reasonable request.

Keywords

high mass loading, laser scribing, oxygen vacancy, spin regulation, supercapacitors

Received: September 14, 2023
Revised: October 10, 2023
Published online:

[1] C. Choi, D. S. Ashby, D. M. Butts, R. H. Deblock, Q. Wei, J. Lau, B. Dunn, *Nat. Rev. Mater.* **2020**, *5*, 5.
[2] Y. Wang, Y. Song, Y. Xia, *Chem. Soc. Rev.* **2016**, *45*, 5925.
[3] a) M. Toupin, T. Brousse, D. Bélanger, *Chem. Mat.* **2004**, *16*, 3184; b) Y. Wan, Y. Li, K. Wang, H. Liu, H. Hu, M. Wu, *Adv. Energy Sustain. Res.* **2022**, *3*, 2100221.
[4] M. Huang, F. Li, F. Dong, Y. X. Zhang, L. L. Zhang, *J. Mater. Chem. A* **2015**, *3*, 21380.
[5] a) J. Li, J. Ma, Z. Ma, E. Zhao, K. Du, J. Guo, T. Ling, *Adv. Energy Sustain. Res.* **2021**, *2*, 2100034; b) S. Yao, S. Wang, R. Liu, X. Liu, Z. Fu, D. Wang, H. Hao, Z. Yang, Y.-M. Yan, *Nano Energy* **2022**, *99*, 107391.
[6] a) W. T. Hong, M. Risch, K. A. Stoerzinger, A. Grimaud, J. Suntivich, Y. Shao-Horn, *Energy Environ. Sci.* **2015**, *8*, 1404; b) J. Suntivich, K. J. May, H. A. Gasteiger, J. B. Goodenough, Y. Shao-Horn, *Science* **2011**, *334*, 1383; c) J. Hwang, R. R. Rao, L. Giordano, Y. Katayama, Y. Yu, Y. Shao-Horn, *Science* **2017**, *358*, 751.

[7] a) Y. Sun, X. Ren, S. Sun, Z. Liu, S. Xi, Z. J. Xu, *Angew. Chem., Int. Ed.* **2021**, *60*, 14536; b) C. Y. Zhang, C. Zhang, G. W. Sun, J. L. Pan, L. Gong, G. Z. Sun, J. J. Biendicho, L. Balcells, X. L. Fan, J. R. Morante, J. Y. Zhou, A. Cabot, *Angew. Chem., Int. Ed.* **2022**, *61*, e202211570.
[8] Y. Zhu, W. Zhou, J. Yu, Y. Chen, M. Liu, Z. Shao, *Chem. Mat.* **2016**, *28*, 1691.
[9] S. Zhou, X. Miao, X. Zhao, C. Ma, Y. Qiu, Z. Hu, J. Zhao, L. Shi, J. Zeng, *Nat. Commun.* **2016**, *7*, 11510.
[10] a) Z. Wang, S. Shen, Z. Lin, W. Tao, Q. Zhang, F. Meng, L. Gu, W. Zhong, *Adv. Funct. Mater.* **2022**, *32*, 2112832; b) S. Yao, R. Zhao, S. Wang, Y. Zhou, R. Liu, L. Hu, A. Zhang, R. Yang, X. Liu, Z. Fu, D. Wang, Z. Yang, Y.-M. Yan, *Chem. Eng. J.* **2022**, *429*, 132521.
[11] X. Wei, S. Song, W. Cai, X. Luo, L. Jiao, Q. Fang, X. Wang, N. Wu, Z. Luo, H. Wang, Z. Zhu, J. Li, L. Zheng, W. Gu, W. Song, S. Guo, C. Zhu, *Chem* **2023**, *9*, 181.
[12] a) Q. Lv, Z. Zhu, Y. Ni, J. Geng, F. Li, *Angew. Chem., Int. Ed.* **2022**, *61*, e202114293; b) H. Li, J. Wang, R. Qi, Y. Hu, J. Zhang, H. Zhao, J. Zhang, Y. Zhao, *Appl. Catal. B-Environ.* **2021**, *285*, 119778.
[13] Y. Zhang, Y. Hu, Z. Wang, T. Lin, X. Zhu, B. Luo, H. Hu, W. Xing, Z. Yan, L. Wang, *Adv. Funct. Mater.* **2020**, *30*, 2004172.
[14] A. Zhang, R. Gao, L. Hu, X. Zang, R. Yang, S. Wang, S. Yao, Z. Yang, H. Hao, Y.-M. Yan, *Chem. Eng. J.* **2021**, *417*, 129186.
[15] J. Wang, S.-J. Kim, J. Liu, Y. Gao, S. Choi, J. Han, H. Shin, S. Jo, J. Kim, F. Ciucci, H. Kim, Q. Li, W. Yang, X. Long, S. Yang, S.-P. Cho, K. H. Chae, M. G. Kim, H. Kim, J. Lim, *Nat. Catal.* **2021**, *4*, 212.
[16] P. L. Yadav, A. R. Shelke, H.-T. Wang, K.-H. Chen, W.-X. Lin, C.-W. Li, M.-Y. Chen, P.-H. Yeh, C.-L. Dong, M. Qorbani, Y.-C. Huang, J.-W. Chiou, H.-M. Tsai, P. M. Kadam, K.-H. Chen, L.-C. Chen, W.-F. Pong, *ACS Appl. Energ. Mater.* **2023**, *6*, 6443.
[17] a) J. Yan, Y. Wang, Y. Zhang, S. Xia, J. Yu, B. Ding, *Adv. Mater.* **2021**, *33*, 2007525; b) L. Zhang, A. Cheruvathur, C. Biz, M. Fianchini, J. Gracia, *Phys. Chem. Chem. Phys.* **2019**, *21*, 2977.
[18] T. Xiong, Z. G. Yu, H. Wu, Y. Du, Q. Xie, J. Chen, Y.-W. Zhang, S. J. Pennycook, W. S. V. Lee, J. Xue, *Adv. Energy Mater.* **2019**, *9*, 1803815.
[19] a) J. Lin, Z. Peng, Y. Liu, F. Ruiz-Zepeda, R. Ye, E. L. G. Samuel, M. J. Yacaman, B. I. Yakobson, J. M. Tour, *Nat. Commun.* **2014**, *5*, 5714; b) X.-T. Sun, Y. Wan, B. Wang, Q. Xu, X.-L. Teng, H.-Y. Liu, Y.-J. Wang, S.-W. Guo, C.-H. Wu, H. Hu, M.-B. Wu, *Rare Met.* **2022**, *41*, 4094; c) H. Hu, Q. Li, L. Li, X. Teng, Z. Feng, Y. Zhang, M. Wu, J. Qiu, *Matter* **2020**, *3*, 95.
[20] Y. Li, D. X. Luong, J. Zhang, Y. R. Tarkunde, C. Kittrell, F. Sargunaraj, Y. Ji, C. J. Arnusch, J. M. Tour, *Adv. Mater.* **2017**, *29*, 1700496.
[21] H. Yang, Y. Wan, K. Sun, M. Zhang, C. Wang, Z. He, Q. Li, N. Wang, Y. Zhang, H. Hu, M. Wu, *Adv. Funct. Mater.* **2023**, *33*, 2215076.
[22] a) H. Zeng, X.-W. Du, S. C. Singh, S. A. Kulinich, S. Yang, J. He, W. Cai, *Adv. Funct. Mater.* **2012**, *22*, 1333; b) Z. Li, C.-K. Dong, J. Yang, S.-Z. Qiao, X.-W. Du, *J. Mater. Chem. A* **2016**, *4*, 2699.
[23] a) A. Zhang, R. Zhao, L. Hu, R. Yang, S. Yao, S. Wang, Z. Yang, Y.-M. Yan, *Adv. Energy Mater.* **2021**, *11*, 2101412; b) V. P. Santos, M. F. R. Pereira, J. J. M. Órfão, J. L. Figueiredo, *Appl. Catal. B-Environ.* **2010**, *99*, 353.
[24] W. Hong, M. Shao, T. Zhu, H. Wang, Y. Sun, F. Shen, X. Li, *Appl. Catal. B-Environ.* **2020**, *274*, 119088.
[25] a) J. Li, C. Shu, C. Liu, X. Chen, A. Hu, J. Long, *Small* **2020**, *16*, 2001812; b) J. Sun, N. Guo, Z. Shao, K. Huang, Y. Li, F. He, Q. Wang, *Adv. Energy Mater.* **2018**, *8*, 1800980.
[26] S. Lee, W. Jin, S. H. Kim, S. H. Joo, G. Nam, P. Oh, Y.-K. Kim, S. K. Kwak, J. Cho, *Angew. Chem., Int. Ed.* **2019**, *58*, 10478.
[27] Y. Zhao, G. Chen, T. Bian, C. Zhou, G. I. N. Waterhouse, L.-Z. Wu, C.-H. Tung, L. J. Smith, D. O'hare, T. Zhang, *Adv. Mater.* **2015**, *27*, 7824.
[28] P. Simon, Y. Gogotsi, *Nat. Mater.* **2008**, *7*, 845.
[29] T. Zhai, S. Xie, M. Yu, P. Fang, C. Liang, X. Lu, Y. Tong, *Nano Energy* **2014**, *8*, 255.
[30] S. Fleischmann, J. B. Mitchell, R. Wang, C. Zhan, D.-E. Jiang, V. Presser, V. Augustyn, *Chem. Rev.* **2020**, *120*, 6738.
[31] Y. Chen, C. Zhou, G. Liu, C. Kang, L. Ma, Q. Liu, *J. Mater. Chem. A* **2021**, *9*, 2872.
[32] Z. Peng, S. Li, Y. Huang, J. Guo, L. Tan, Y. Chen, *Adv. Funct. Mater.* **2022**, *32*, 2206539.
[33] G. Nagaraju, Y. H. Ko, S. M. Cha, S. H. Im, J. S. Yu, *Nano Res.* **2016**, *9*, 1507.
[34] a) F. Jing, Z. Ma, J. Wang, Y. Fan, X. Qin, G. Shao, *Chem. Eng. J.* **2022**, *435*, 135103; b) Y.-K. Hsu, Y.-C. Chen, Y.-G. Lin, L.-C. Chen, K.-H. Chen, *Chem. Commun.* **2011**, *47*, 1252.
[35] S. Mukherjee, H. D. Yang, A. K. Pal, S. Majumdar, *J. Magn. Magn. Mater.* **2012**, *324*, 1690.
[36] a) Y. Wang, Y.-Z. Zhang, D. Dubbink, J. E. Ten Elshof, *Nano Energy* **2018**, *49*, 481; b) P. Zhao, N. Wang, M. Yao, H. Ren, W. Hu, *Chem. Eng. J.* **2020**, *380*, 122488; c) M. Lu, Z. Zhang, L. Kang, X. He, Q. Li, J. Sun, R. Jiang, H. Xu, F. Shi, Z. Lei, Z.-H. Liu, *J. Mater. Chem. A* **2019**, *7*, 12582; d) R. Zhong, M. Xu, N. Fu, R. Liu, A. Zhou, X. Wang, Z. Yang, *Electrochim. Acta* **2020**, *348*, 136209; e) Q. Zhang, C. Zhang, F. Yang, J. Yu, H. Dong, J. Sui, Y. Chen, L. Yu, L. Dong, *Ceram. Int.* **2022**, *48*, 13996; f) Q. Zhang, F. Yang, C. Zhang, H. Dong, J. Sui, L. Yu, Y. Chen, J. Yu, L. Dong, *Appl. Surf. Sci.* **2021**, *551*, 149417; g) P. Du, Y. Dong, Y. Dong, X. Wang, H. Zhang, *J. Mater. Sci.* **2022**, *57*, 3497; h) M. Li, Z. Li, X. Wang, N. Fu, Z. Yang, *J. Electroanal. Chem.* **2022**, *919*, 116556; i) Y. Wang, J. Xiao, T. Zhang, L. Ouyang, S. Yuan, *ACS Appl. Mater. Interfaces* **2021**, *13*, 45670; j) Y. Zhu, H. Xu, P. Chen, Y. Bao, X. Jiang, Y. Chen, *Electrochim. Acta* **2022**, *413*, 140146; k) Z. Liu, H. Li, X. Liu, J. Guo, S. Zhang, Y. Lu, *J. Energy Storage* **2023**, *67*, 107527.